Role of the brittle–ductile transition on fault activation

C. Doglioni [a,c,*], S. Barba [b], E. Carminati [a,c], F. Riguzzi [b,*]

[a] Dipartimento di Scienze della Terra, Università Sapienza, Roma, Italy
[b] Istituto Nazionale di Geofisica e Vulcanologia, CNT, via di Vigna Murata 605, Roma 00143, Italy
[c] Istituto di Geologia Ambientale e Geoingegneria, CNR, Roma, Italy

ABSTRACT

We model a fault cross-cutting the brittle upper crust and the ductile lower crust. In the brittle layer the fault is assumed to have stick–slip behaviour, whereas the lower ductile crust is inferred to deform in a steady-state shear. Therefore, the brittle–ductile transition (BDT) separates two layers with different strain rates and structural styles. This contrasting behaviour determines a stress gradient at the BDT that is eventually dissipated during the earthquake. During the interseismic period, along a normal fault it should form a dilated hinge at and above the BDT. Conversely, an over-compressed volume should rather develop above a thrust plane at the BDT. On a normal fault the earthquake is associated with the coseismic closure of the dilated fractures generated in the stretched hangingwall during the interseismic period. In addition to the shear stress overcoming the friction of the fault, the brittle fault moves when the weight of the hangingwall exceeds the strength of the dilated band above the BDT. On a thrust fault, the seismic event is instead associated with the sudden dilation of the previously over-compressed volume in the hangingwall above the BDT, a mechanism requiring much more energy because it acts against gravity. In both cases, the deeper the BDT, the larger the involved volume, and the bigger the related magnitude.

We tested two scenarios with two examples from L'Aquila 2009 (Italy) and Chi-Chi 1999 (Taiwan) events. GPS data, energy dissipation and strain rate analysis support these contrasting evolutions. Our model also predicts, consistently with data, that the interseismic strain rate is lower along the fault segment more prone to seismic activation.

© 2010 Elsevier B.V. All rights reserved.

1. Introduction

Fault activation is crucial for the understanding of earthquakes and their prediction (e.g., Scholtz, 1990; Stein and Wysession, 2003; Peresan et al., 2005). Earthquakes are usually interpreted as the rupture of an asperity along a fault, when the shear stress overcomes the fault strength. But why do faults move episodically? Why is seismicity not more randomly distributed if an earthquake is simply associated with an asperity, which should be smeared out after fault motion? The origin of the earthquake recurrence or seismic cycle (e.g., Thatcher and Rundle, 1979; Savage, 1983; Cattin and Avouac, 2000; Sieh et al., 2008), consisting of a long interseismic period followed by a coseismic (and postseismic) period, remains quite obscure. The length of the interseismic period between two earthquakes along the same fault has been proposed to be controlled by a number of physical parameters, e.g., the relative velocity between the two walls of the fault, the composition of the crust, the mineralogy and foliation of the fault rocks, the morphology and length of the fault plane, the thermal state, the friction on the fault, the fluid pore-pressure, etc. (e.g., Scholtz, 1990; Collettini et al., 2009). All these parameters entail first a long, static accumulation of energy during the interseismic period, which is eventually radiated coseismically when the friction on the fault has overcome. In this article we contribute to this topic with a geological model to explain the activation of a crustal fault, where the aforementioned physical parameters could determine the timescale of the recurrence or the magnitude. In particular, we investigate the role of the brittle–ductile transition (BDT) in the evolution of crustal seismicity. The BDT depth generally represents the lower limit of most crustal seismicity. We propose a model that links the continuous ductile deformation at depth with the brittle episodic behaviour of shallow crustal layers, and show how the BDT may play a triggering role in fault movement. The model is tested numerically and applied to two areas where normal fault and thrust related earthquakes occurred, i.e., in the central Apennines (2009) and Taiwan (1999). GPS interseismic and coseismic data, dissipated energy from the two cases are shown to be consistent with model predictions, where normal faults and thrusts have opposite behaviour. Similar to the effects of the lithostatic load, which enhances the rupture of normal faults and inhibits faulting along thrusts (Carminati et al., 2004), the two types of faulting are asymmetric in terms of geological and mechanical behaviour.

* Corresponding authors.
 E-mail addresses: carlo.doglioni@uniroma1.it (C. Doglioni), riguzzi@ingv.it (F. Riguzzi).
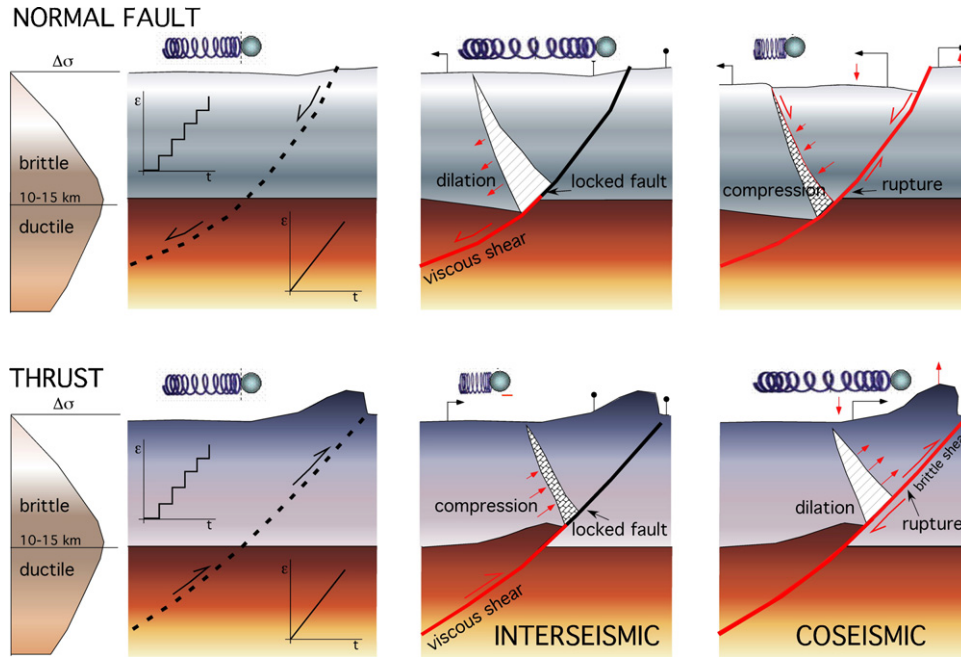
Fig. 1. Assuming a steady stated strain rate in the ductile lower crust, stick–slip motion in the brittle upper crust, tensional and compressional faults generate opposite kinematics and mechanic evolution. In the tensional tectonic environment, the triangle of crust above the BDT remains "suspended" while a dilated area forms during the interseismic period. Once shear stress along the locked part of the fault becomes larger than fault strength, the hangingwall will collapse. Conversely, along a thrust plane, an area over-compressed separates the ductile shear from the overlying locked fault during the interseismic period. The hangingwall is expelled as a compressed spring during the coseismic period.

2. Geological model

It is widely accepted in the literature that the rheology of the crust can be simplified with an upper brittle layer and a deeper ductile crust (e.g., Rutter, 1986). The transition between the brittle shallow crust and the ductile deep crust is thought to determine differing tectonic behaviours between the two domains. The steady state deformation in the ductile layer is, in fact, at odds with the stick–slip behaviour of the shallower brittle levels. The constant strain rates measured by GPS during interseismic periods (e.g., Kreemer et al., 2002) suggest that the locked status of faults in the brittle layer does not inhibit continuous ductile shear below the BDT. Therefore, we speculate that the episodic stick–slip behaviour of the brittle crust coexists with steady-state shear in the lower crust. In the volume across the BDT, strain is transferred from one mechanism to the other. This differential behaviour implies that during the interseismic period the absence of motion in the brittle layer contrasting with the continuous slip in the ductile layer generates a pressure gradient, which will be eventually dissipated during the activation of the fault in the brittle segment at the coseismic stage.

We assume a simple fault plane cross-cutting both the brittle and the ductile layers of the crust. In normal faulting, deep ductile deformation generates a dilation at the interface with the brittle shallow locked part of the fault. Dilatancy (i.e., the phenomenon in which fractures and cracks form and open when rocks are stressed; e.g., Frank, 1965) should reach its maximum at the BDT. Conversely, compression should form in the footwall of the normal fault. One example could be the antithetic normal fault that slipped during the 40 s sub-event of the Irpinia 1980 earthquake (Pingue and De Natale, 1993). During the coseismic stage, the hangingwall instantaneously subsides down, closing the fractures in the dilated volume (e.g., Axen, 1999). This can be explained by the weight of the brittle hangingwall that overcomes the strength of the weakened dilated band (Fig. 1). The triangle suddenly falls when the shear stress along the locked part of the fault is equal to the fault strength. Moreover the area stretched during the interseismic period may become the location for the development of a conjugate normal fault (Melosh and Williams, 1989, Fig. 1). Cracks and veins close to the BDT transition have been described by Nuchter and Stockhert (2008). They inferred their generation during the coseismic stage, but such veins could also have formed during the interseismic period.

Unlike the normal fault case, along a thrust the hangingwall above the BDT is over-compressed during the interseismic, and should dilate at the coseismic stage (Fig. 1). The opposite distribution of stress is expected in the footwall. During the coseismic stage, elastic rebound is expected with uplift of the hangingwall along the brittle segment of the thrust, and internal subsidence should ensue above the BDT where some dilatancy should develop instantaneously (Fig. 1). This is compatible with the data and model presented by Burrato et al. (2003) for fault-propagation folding and it has been detected during the great Sumatra earthquake (Meltzner et al., 2006).

Our model can be simplified as follows. Let us imagine a spring located across the BDT, with its terminations attached to the ductile and the brittle parts of the hangingwall. During the interseismic period, along a normal fault the motion of the ductile lower part will elongate the spring and accumulate energy. In the coseismic stage, energy will be released and the spring will contract (Fig. 1). Along a thrust, the opposite behaviour is expected, i.e., the spring will be shortened during the interseismic, whereas it will extend during the coseismic stage (Fig. 1).

3. Numerical modelling

In order to evaluate the physical feasibility of the proposed geological model, the results of some numerical simulations will be discussed. Finite element dynamic modelling was performed using the commercial COMSOL Multiphysics 3.5 software (http://www.comsol.com/).
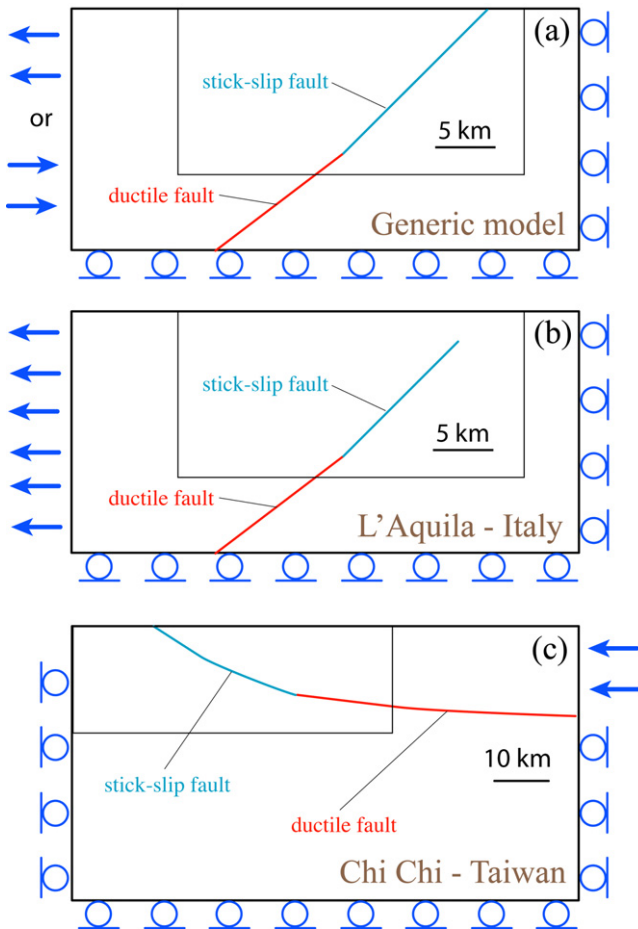
Fig. 2. Geometry and boundary conditions for the conceptual model (a), for the L'Aquila event (b), and for the Chi-Chi event (c). The thin-line rectangle shows the portion of the model shown in Figs. 3, 8 and 12.

3.1. Model setup

The model adopts 2D plane strain approximation and all the layers are described by an elastic rheology (Young's Modulus: 2×10^{11} Pa; Poisson's ratio: 0.33). The elastic constants do not affect significantly the pattern of the stress field, which is our main interest. However, we tested our model in the Poisson's ratio range of 0.27–0.33, and found that such changes bear, in a first approximation, negligible effects on the magnitude and orientation of stresses. The generic model geometry is shown in Fig. 2a. The model is 20 km deep and 42 km wide and is separated in two distinct parts by a 45° dipping plane to simulate both normal faulting or thrust earthquakes. The finite element grid is made of 12,465 triangular linear Lagrange elements (14,517 degrees of freedom). Gravity is applied as a body force to all the elements. A constant density of 2850 kg m^{-3} is assigned to all the elements and the gravitational acceleration is kept constant (9.81 m s^{-2}) with depth. The behaviour of the fault is modelled as a contact body (contact pairs in COMSOL's nomenclature) and is varied (locked or unlocked) in space and time. Unlocked sectors of the fault are modelled as no-friction planes, while locked portions are modelled as identity pairs. The deeper (>9 km) part of the fault is always modelled as unlocked, simulating the ductile (aseismic) slip of faults at depth.

Modelling is performed in three separate stages. At first gravity is applied instantaneously and, as a consequence, a laterally variable (up to ca. 45 m) collapse of the surface occurs. During this stage the following boundary conditions are applied: only horizontal slip is allowed along the lower boundary; only vertical slip is allowed

along the lateral boundaries; the surface is left free. Minor problems in the numerical solution are due to the fact that the bottom boundary is free to slip and the freely slipping ductile shear zone intersects the bottom boundary. At this intersection the solution is not accurate. However, the intersection is sufficiently far from the area of interest.

The free-slip boundary condition at the bottom of the model actually implies that the crustal blocks slip over a horizontal detachment. Of course, this assumption stems from the difficulty of transitioning between localized and distributed deformation. This boundary condition is justified by the fact that at a depth of 20 km the crust is expected to behave plastically.

During this period, the seismogenic portion of the fault (i.e. in the 0–9 km range) is left unlocked. The resulting stress field is used as initial state for the following stages. In a second stage, a displacement of 5 m (directed to the left for normal faulting and to the right for thrust faulting) is imposed in 10 steps to the left boundary of the model. The remaining boundary conditions are unvaried. The seismogenic portion of the fault is kept locked, so to simulate the stress accumulation during the interseismic period of the seismic cycle. In a third stage the seismogenic fault is unlocked and no further displacement is imposed to the left boundary of the model to simulate the coseismic stress field. It is here stressed that rupture is imposed a priori, i.e., no self-consistent failure criterion is assumed. This means that, with our model, we investigate the different stresses and strain distribution associated with interseismic and coseismic stages, rather than assessing what processes control the timing of rupture.

3.2. Modelling results

In order to appreciate the effect on the stress field of stretching in interseismic and coseismic periods, we show the dilation (Fig. 3a, b, g and h), the shear stress σ_{xy} (Fig. 3c, d, i and l) and the principal stress axes (blue compression and red tension) (Fig. 3e, f, m and n) resulting from the difference between the final stage stress (gravity and displacement applied) and the initial stage stress (only gravity applied).

During extension prior to normal faulting, dilation occurs in the fault hangingwall during the interseismic stage (Fig. 3a) whereas fracture closure occurs in the footwall right below the lock-up point of the fault. Both deformation fields disappear during the coseismic stage (Fig. 3b), together with the significant decrease of the shear stress. Fig. 3e shows that during interseismic phases (after 5 m of displacement), stretching generally induces horizontal tension with minor vertical compression. In the hangingwall of the slipping portion of the fault, tension is fault parallel, while fault parallel compression occurs in the footwall. Fig. 3f shows that the coseismic period (after the unlocking of the fault) is characterized by a stress drop (also evident comparing Fig. 3c and d). During coseismic stages, oblique tension (perpendicular to the fault plane) and fault-parallel compression are predicted in the hangingwall at depth (Fig. 3f). Horizontal compression occurs in the shallowmost 2 km of the hangingwall. Fault-parallel compression is predicted for the footwall at 0–4 km depths whereas fault-parallel tension occurs at deeper depths.
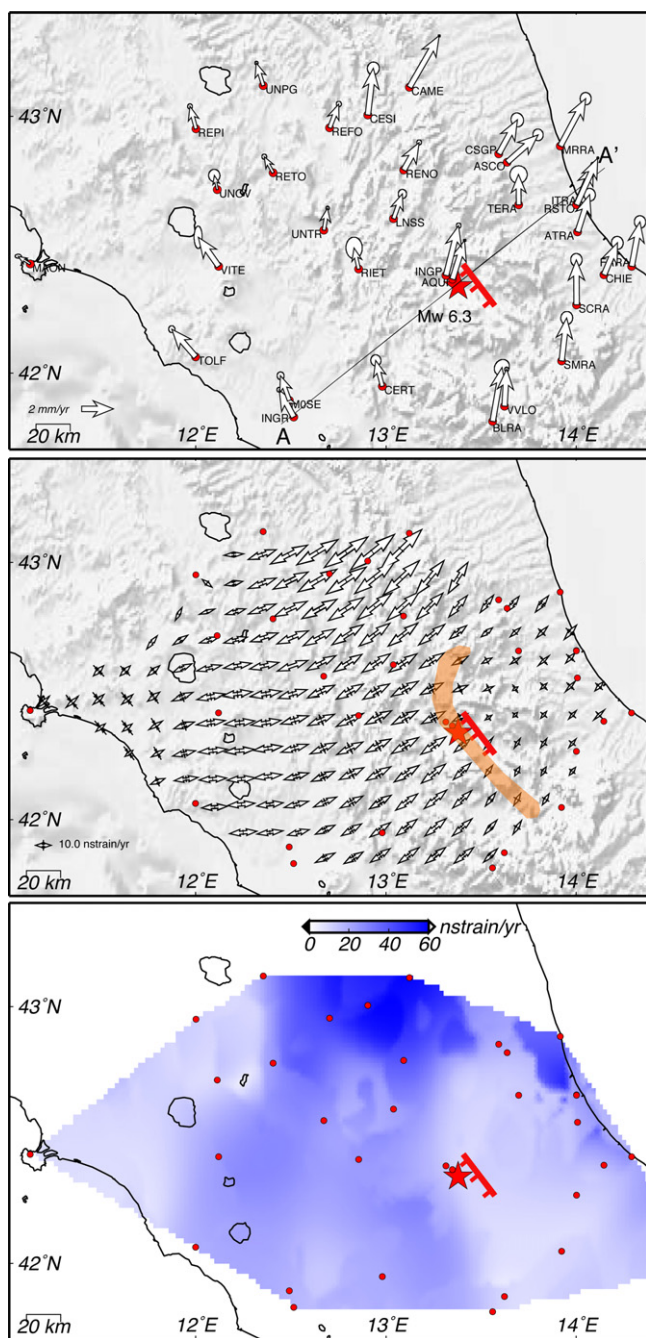
During compression prior to thrusting, fracture closure is predicted for a wide area in the hangingwall (Fig. 3i), whereas a small portion of the footwall is predicted to dilate. At the coseismic stage, both dilation and contraction are released (Fig. 3l). Also in this case the shear stress accumulated during the interseismic stage is coseismically released. During the interseismic stage (Fig. 3m), overall horizontal compression and no significant vertical stresses are predicted with the exception of the footwall at depth deeper than 7 km, where vertical tension (increasing with depth) is predicted. Again, a stress drop occurs during coseismic stages (after the
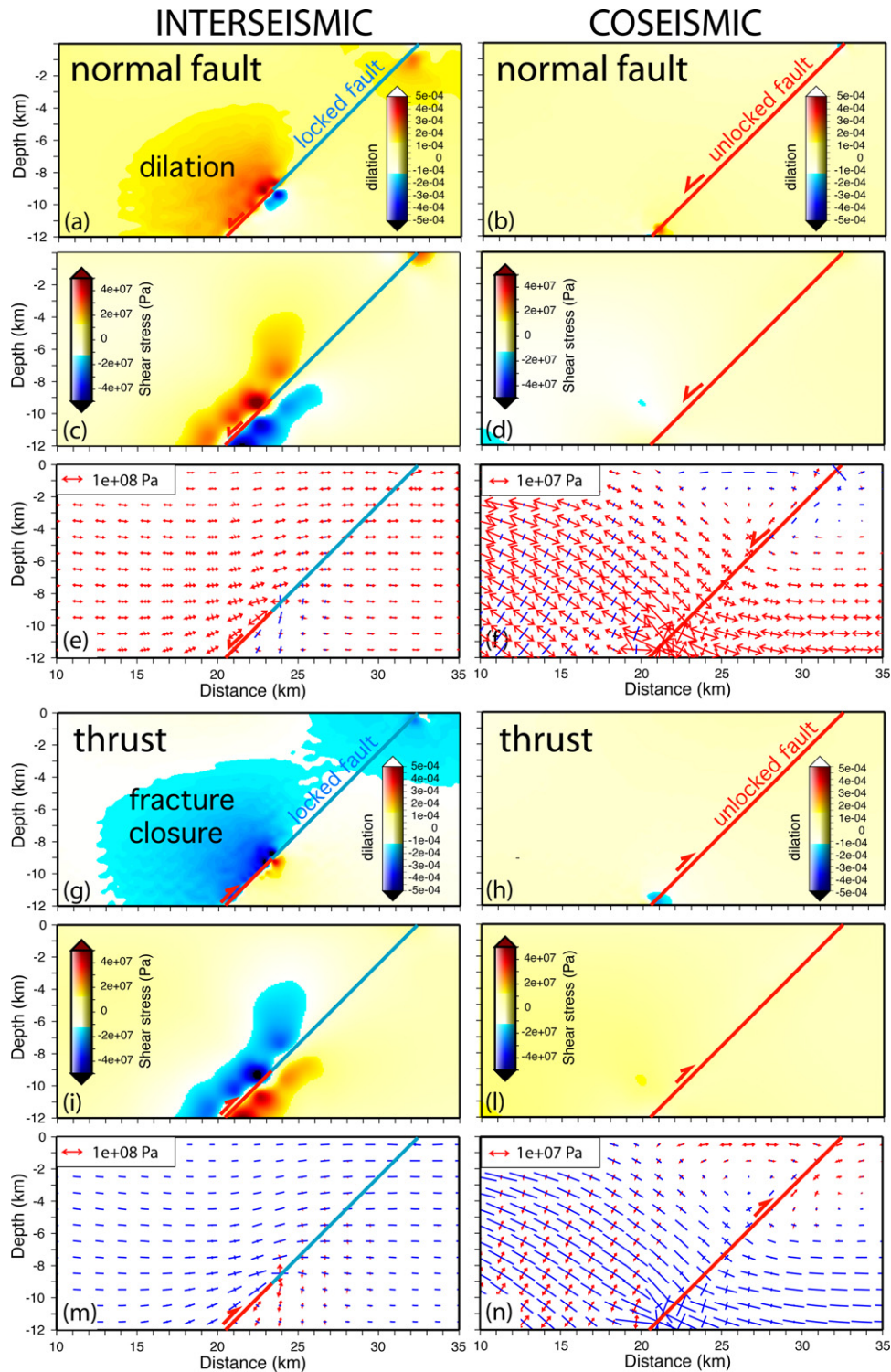
Fig. 3. Along a normal fault, a dilation area occurs in the hangingwall during interseismic stages (a) and disappears in coseismic stages (b), characterized by significant stress drop (compare the shear stress distribution of panels (c) and (d). The axes of principal stresses for interseismic stages (e) and coseismic stages (f) are also shown (blue compression and red tension). Conversely, along a thrust a contraction area is predicted at the tip of the ductile segment of the fault (g) during the interseismic period, associated with large values of shear stress (i). The brittle segment, unlocked during the coseismic period, shows a dilation area at its base (l). The axes of principal stresses for interseismic (m) and coseismic (n) stages have opposite trends. In red are the active segments of the faults. (For interpretation of the references to colour in this figure legend, the reader is referred to the web version of the article.)

unlocking of the fault), as shown in Fig. 3n. Oblique (fault-normal) compression is predicted in the hangingwall with the exception of the shallowmost 2 km where horizontal tension occurs. Fault-parallel tension is predicted for a wide area in the hangingwall. In the footwall, fault-parallel tension is predicted for the shallowmost 4 km and compression at deeper depths.

The numerical model has the limit that the fault offset goes to zero almost instantaneously at the BDT, whereas in nature this may be distributed over a transfer zone possibly thicker than one or more km. The numerical model shows two relevant results: (1) the concentration of the strain and shear stress at the BDT during the interseismic period (i.e., where the brittle locked fault transition to

Fig. 4. Upper panel: GPS interseismic velocity field in central Italy and L'Aquila area. The line indicates the trace of the sections shown in Fig. 5, crossing the fault that generated the earthquake. The star is the April 6th event. Middle panel: strain rate principal axes on a regular grid based on the interseismic velocities. The shaded area represents the high strain rate gradient separating in the north the region which underwent the 1997–1998 Umbria-Marche seismic event, and to the southeast the L'Aquila area before the 2009 quake. Lower panel: map of the extension rate. The northern area is in a post-seismic state, whereas the L'Aquila area is at the interseismic stage (see Fig. 1, upper panel), and the April earthquake developed in the area of lower extensional strain rate.

Table 1
Interseismic velocities of continuous GPS sites.

Site	Lon. (°)	Lat. (°)	East (mm/y)	North (mm/y)	±E (mm/y)	±N (mm/y)	Corr.
AQUI	13.350	42.368	0.76	2.43	0.08	0.07	−0.01
ASCO	13.637	42.823	1.93	1.71	0.33	0.37	−0.03
ATRA	14.007	42.552	0.75	2.33	0.36	0.40	−0.03
BLRA	13.560	41.810	0.58	3.39	0.47	0.50	0.15
CAME	13.124	43.112	1.86	3.23	0.06	0.07	−0.01
CERT	12.982	41.949	−0.42	1.61	0.32	0.35	−0.04
CESI	12.905	43.005	0.34	2.92	0.38	0.40	0.03
CHIE	14.145	42.385	0.84	2.00	0.37	0.41	−0.03
CSGP	13.592	42.855	1.17	2.13	0.40	0.44	−0.07
FRES	14.669	41.974	0.81	3.64	0.22	0.25	−0.04
FRRA	14.292	42.418	0.51	2.78	0.36	0.39	−0.03
INGP	13.316	42.383	0.79	3.12	0.15	0.16	−0.04
INGR	12.515	41.828	−0.91	1.71	0.14	0.15	−0.01
ITRA	14.002	42.659	1.04	2.47	0.16	0.17	−0.02
LNSS	13.040	42.603	0.55	1.56	0.26	0.29	−0.01
M0SE	12.493	41.893	−0.56	1.55	0.22	0.24	−0.02
MAON	11.131	42.428	−0.76	0.47	0.20	0.12	−0.02
MRRA	13.916	42.885	1.59	2.97	0.35	0.39	−0.02
REFO	12.704	42.956	0.57	1.49	0.16	0.17	−0.01
RENO	13.093	42.793	0.97	1.73	0.15	0.16	0.01
REPI	12.002	42.952	−0.38	1.40	0.15	0.17	−0.01
RETO	12.407	42.782	−0.56	1.01	0.15	0.16	0.00
RIET	12.857	42.408	−0.29	1.32	0.52	0.68	−0.01
RSTO	14.002	42.658	1.33	2.93	0.06	0.06	−0.03
SCRA	14.002	42.268	−0.02	2.81	0.36	0.40	−0.02
SMRA	13.924	42.048	0.31	2.69	0.37	0.41	0.02
TERA	13.698	42.657	−0.02	1.90	0.54	0.56	0.02
TOLF	12.000	42.064	−1.50	1.73	0.20	0.22	−0.03
UNOV	12.113	42.716	−0.19	0.89	0.35	0.39	−0.01
UNPG	12.356	43.119	−0.44	1.41	0.10	0.11	−0.01
UNTR	12.674	42.559	0.22	1.38	0.11	0.12	−0.01
VITE	12.120	42.418	−1.28	1.82	0.26	0.71	−0.02
VVLO	13.623	41.870	0.13	2.32	0.12	0.14	0.01

primary and secondary porosity of rocks, which are a function of lithology and deformation history. In stratified rocks, porosity is controlled by layering that normally produces strong heterogeneity and anisotropy. However, infinite combinations of porosity, layer thickness and orientation of stratification could be envisaged when addressing a general problem such as we do. For this reason, as normally done in the literature, we chose not to include fluids in the model.

Short of computing actual fluid migration paths, poroelastic solutions for undrained and drained conditions were simulated in the literature by varying the Poisson's ratio (e.g., Peltzer et al., 1998; Fialko, 2004). Poroelastic effects were proven to be important to simulate postseismic deformation induced by poroelastic afterslip (e.g., Peltzer et al., 1998; Masterlak and Wang, 2002; Fialko, 2004). Since we are interested in the changes occurring at the transition between preseismic and coseismic stages, we do not introduce changes in the Poisson's ratio. However, the sensitivity of the model to variations in the Poisson's ratio was evaluated (see the results for the L'Aquila event) and found to be a second order feature (see also Jonsson et al., 2003), in agreement with tomographic studies, which observe Poisson's ratio variations at small (<∼2 km) wavelengths (Di Stefano, pers. comm., 2010).

4. Regional examples

The predictions of both geological and numerical models will be tested against GPS data available for two well studied earthquakes: the M_w 6.3 April 6th 2009 L'Aquila normal fault-related earthquake and the M_w 7.6 September 20th 1999 Chi-Chi thrust-fault related earthquake.

the ductile unlocked slipping fault); (2) the collapse or expulsion of the hangingwall at the coseismic stage provides a change in the state of stress. Both results are in agreement with the geological model.

The model does not account for interaction between rocks and fluids. Including rock–fluid interaction would increase the number of parameters controlling the results, rendering their interpretation unclear. Fluid pressure and flow paths are controlled by the

4.1. Central Apennines extensional belt

The crustal seismicity along the Apennines belt is mainly dominated by normal faulting and confined in the upper crust (Chiarabba et al., 2005), apart from deeper events associated with a westerly directed subducting slab. The lower crust is rather seismically silent. This is consistent with a shallower brittle crust and a deeper ductile crust. On April 6th 2009, a M_l 5.8, M_w 6.3 earthquake occurred close to the city of L'Aquila (Central Apennines, Italy, e.g., Chiarabba et al., 2009); the aftershock distribution evidences a composite extensional structure about 40 km long, trending NW–SE (typical for normal faults in the area; Vezzani and Ghisetti, 1998), and composed of three main segments; the longer one is associated with the mainshock, which nucleated at about 10 km depth, with a sequence of aftershocks reaching up to about 2 km depth, as predicted by the model of Carminati et al. (2004).

In order to verify whether the mainshock occurred close to the BDT as in Fig. 1, regional rheological profiles have been calculated in Barba et al. (2008, 2010). Such profiles indicate a BDT at about 10 km, consistently with seismological observations showing that most of the upper plate crustal seismicity along the Apennines disappears at about 10–15 km (Chiarabba et al., 2005). These rheological profiles justify the assumption made in Fig. 1 of an upper brittle crust and a ductile lower crust in the central Apennines.

The yield shear stress τ_S is given by the minimum between the frictional sliding and the dislocation creep shear stress $\tau_s = \min(\tau_s^{\text{fric}}, \tau_s^{\text{creep}})$. For the tensional regime setting it is

$$\tau_s^{\text{fric}} = \frac{(\rho - \rho_{H_2O})gh}{1 + [\sin(\tan^{-1} \quad \mu)]^{-1}}$$

where g is the gravity acceleration, $\rho = 2600 \text{ kg/m}^3$ the rock density, $\rho_{H_2O} = 1023 \text{ kg/m}^3$ the density of water, and μ is the friction, and

$$\tau_s^{\text{creep}} = \frac{1}{2}A(2\dot{\varepsilon}_s)^{1/n} \quad \exp\left(\frac{B}{T}\right)$$

where $\dot{\varepsilon}_s$ is the shear strain rate, T is the depth-dependent temperature, $A = 2.11 \times 10^6 \text{ Pa s}^{1/3}$, $B = 8625 \text{ K}$ and $n = 2.4$ are rheological parameters (see, e.g., Bird, 1978; Tullis, 1979; A, B and n as in Barba et al., 2008, 2010). We assume the temperature depends on the steady-state heat flow (here 45 mW/m^2), the thermal conductivity (3 W m^{-1} K^{-1}), the volumetric thermal expansion coefficient (2.4×10^{-5}) and the linear radioactive heat production coefficient (8×10^{-7} K^{-1}). For the above listed parameters, for $\dot{\varepsilon}_s = 10^{-15}$ s^{-1} and for the fault friction in the normal range ($\mu = 0.5$–0.8, e.g., Collettini and Sibson, 2001) we obtain a maximum value during the coseismic and early preseismic stages (1 week) of 58–70 MPa at the depth of 12.5 km (33 MPa at the depth of 13.5 km in the case of weak fault). On the other hand, the rheological model predicts a maximum value of 110–120 MPa at the depth of 10 km in the interseismic period.

The seismogenic fault dips about 43–47° to the SW (Chiarabba et al., 2009). The rocks involved in seismicity form a triangular prism of about 3000 km^3; this is the crustal block that has moved down during the earthquake, rupturing at the mainshock, and then gradually collapsed in the following weeks and months to reach a more stable condition.

The interseismic rate of Fig. 4 was obtained through the analysis of 33 GPS permanent stations located in central Italy, in the framework of the processing of all the Italian permanent stations. Site velocities are obtained from the ITRF2005 constrained daily solutions, by simultaneously estimating site velocities, annual signals and sporadic offsets at epochs of instrumental changes, as in Devoti et al. (2008) and Riguzzi et al. (2009).
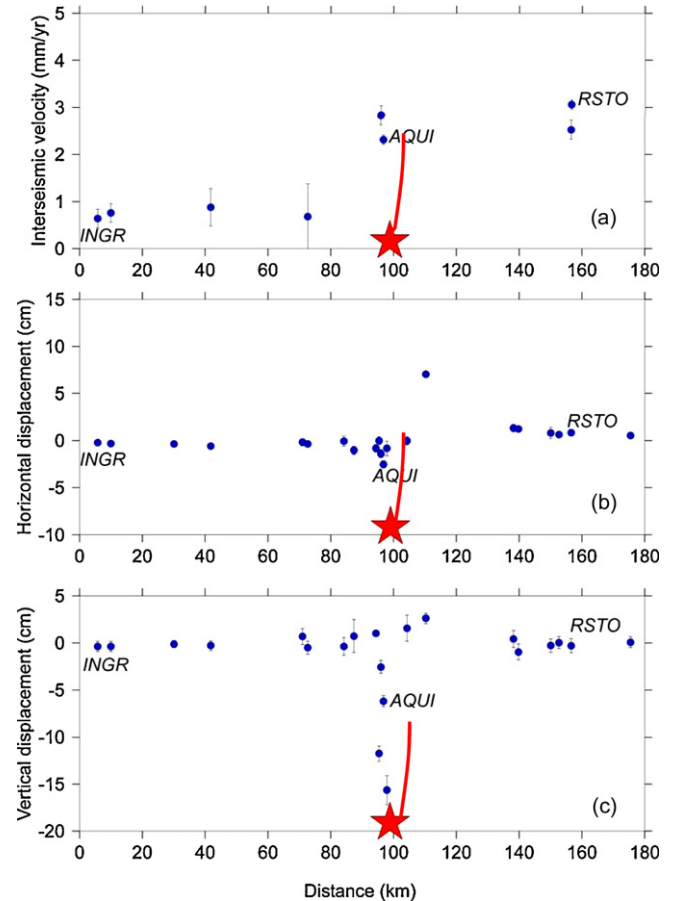

Fig. 5. Interseismic velocities (a), co-seismic horizontal (b) and vertical (c) displacements projected with errors along the section shown in the previous figure, perpendicular to the fault that generated the L'Aquila earthquake. Star, location of the April 6th 2009 mainshock, the earthquake occurred within the western side of the velocity plateau of the interseismic period; the line represents a sketch of the fault section.

The regional velocity field was then removed through the Eurasian fixed reference frame (Fig. 4a and Table 1) defined by the rotation pole and rate estimated in Devoti et al. (2008). The interseismic strain rate is estimated on a regularly spaced grid of 12 km × 12 km using all stations and applying the distance weighted approach $W = \exp(-d^2/2\alpha^2)$, where d is the distance between each node and the stations and α is the smoothing parameter (Shen et al., 1996). Stations within 1α distance contribute for more than 67% to the least squares solution whereas those at distance greater than 3α contribute for less than 1%. These parameters necessarily result in "smearing" of patterns, making it more difficult to relate steep strain gradients to individual structures. Nevertheless this interpolation is useful to model the strain rate when the data are sparse. We take it to represent the interseismic strain rate; the "locked" area near AQUI (L'Aquila) has principal extension rate of $(10 \pm 4) \times 10^{-9}$ strain/y and azimuth 63°; this estimation appears very low if compared with the northernmost Umbria-Marche seismogenic area (Amato et al., 1998) characterized by larger extensional rates of about $(60 \pm 3) \times 10^{-9}$ strain/y and azimuth 45°. In Fig. 4b and c, we show the maps of principal axes of strain rate and the extension rate, respectively. The projection of the GPS horizontal interseismic velocities and errors (Fig. 5a) along the profile A–A' of Fig. 4a shows that the L'Aquila area was characterized by an interseismic velocity of about 2.5 mm/y (between L'Aquila and Rome), outside the event area, and close to zero across the activated fault. Therefore the stronger hazard is localized in an area where the strain rate was lower. In the same figure (Fig. 5b
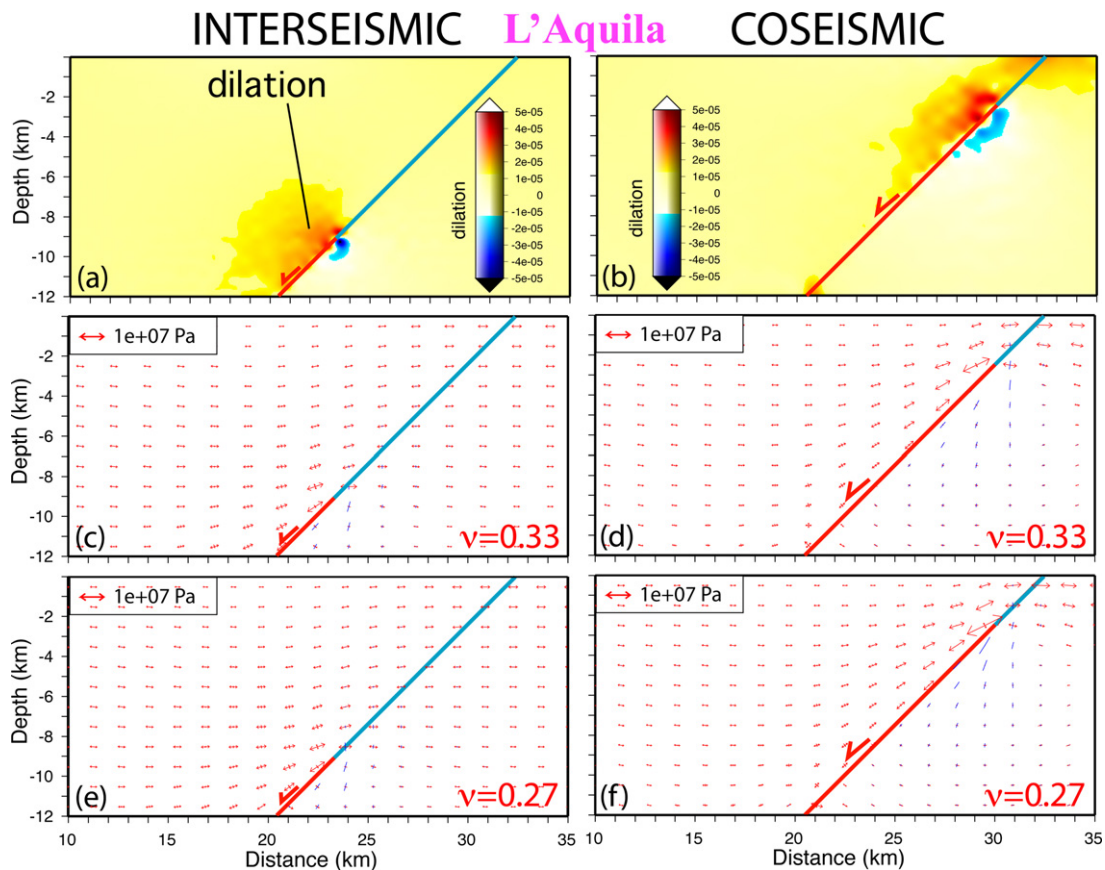
Fig. 6. Dilation (a and b) and principal stress axes (c and d) predicted at interseismic (a and c) and coseismic (b and d) stages by a model built to simulate the L'Aquila event (geometry shown in Fig. 2b), assuming a Poisson's ratio equal to 0.33. More than 30 days foreshocks occurred along an antithetic fault within the dilation area. Panels (e) and (f) show the principal stress axes for the same model, assuming a Poisson's ratio equal to 0.27. Notice that the differences between panels (c and d) and (e and f) are negligible for the purpose of this work.
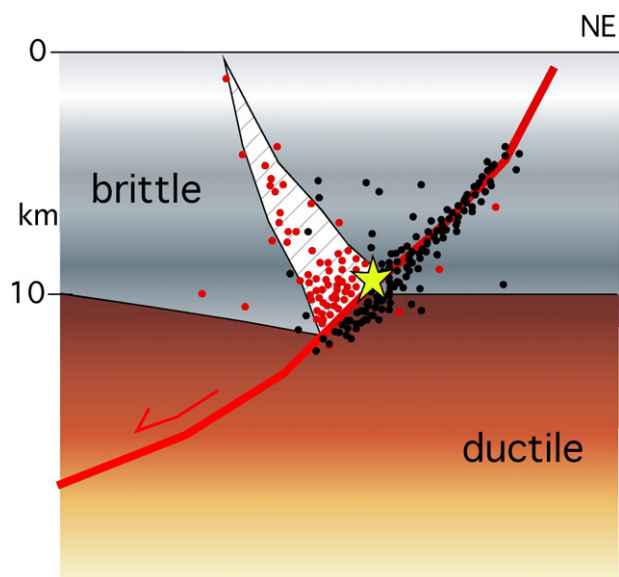
Fig. 7. The foreshocks (red dots) occurred in the dilated band above the BDT, indicating the initial collapse of the hangingwall over the weakened area as predicted by the model. On the other hand, the aftershocks (black dots) mostly developed along the coseismic activated normal fault, and the settlement of the fallen hangingwall. Location of the events after Chiarabba et al. (2009) and Di Luccio et al. (2010). (For interpretation of the references to colour in this figure legend, the reader is referred to the web version of the article.)
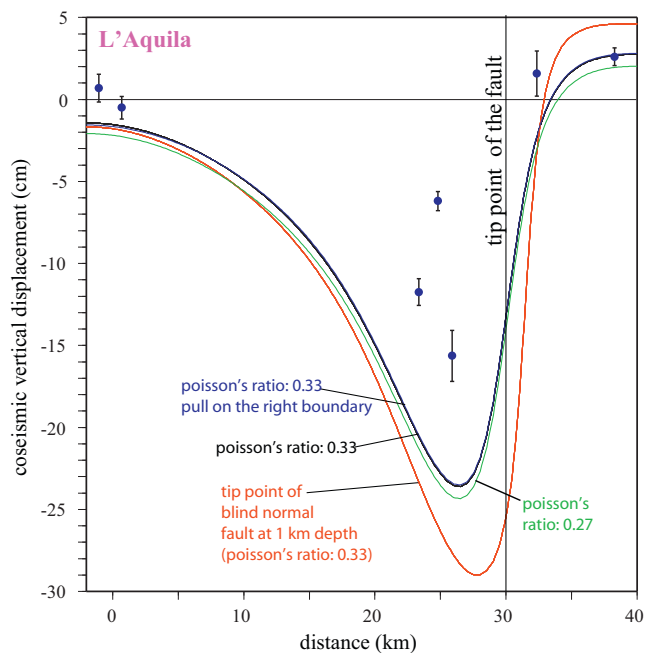
Fig. 8. L'Aquila event: comparison between model and observations. The continuous lines are the coseismic vertical motions predicted at the surface by the model (geometry shown in Fig. 2b). The blue dots are the coseismic displacements with errors estimated at the nearest GPS sites. (For interpretation of the references to colour in this figure legend, the reader is referred to the web version of the article.)
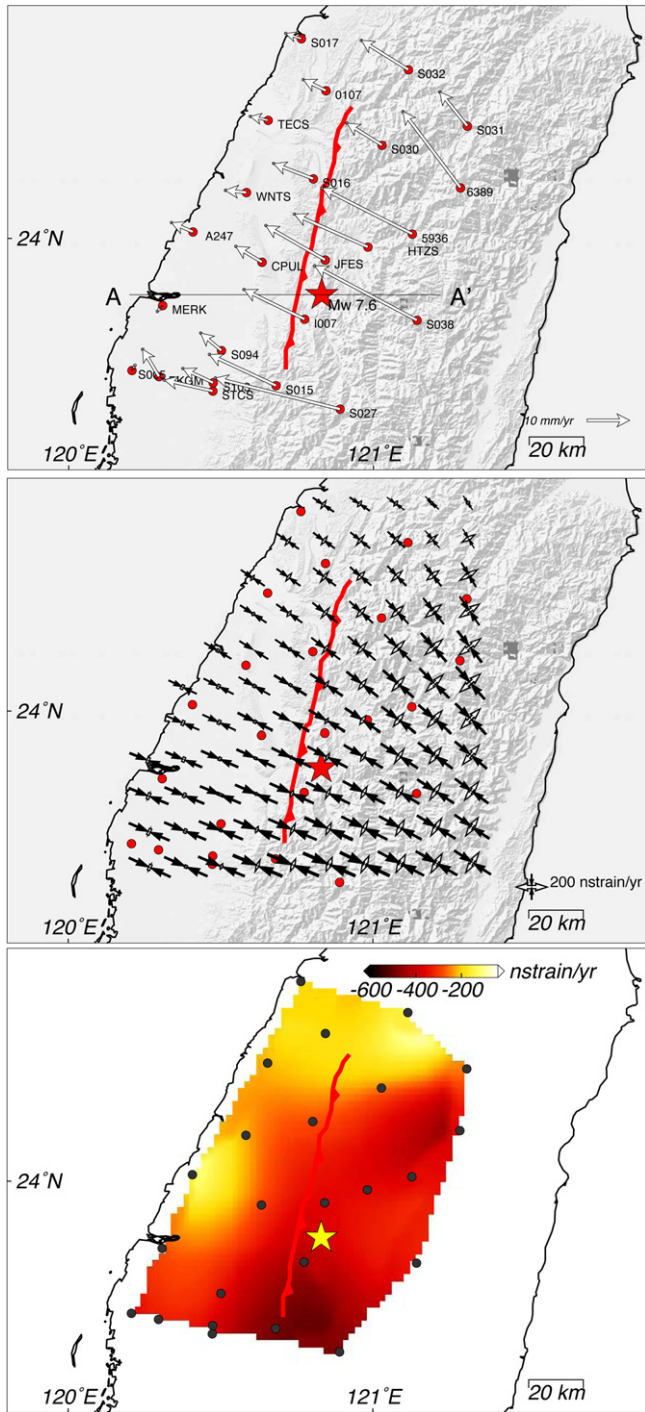
Fig. 9. Upper panel: interseismic velocity field in Taiwan, GPS data from Yu et al. (2001). The line indicates the trace of the sections shown in Fig. 10, crossing the fault that generated the earthquake. Middle panel: strain rate principal axes on a regular grid obtained from the interseismic velocity field. Lower panel: shortening rate of the region. The Chi-Chi 1999 earthquake was generated in an area of relative lower strain rate. Lower shortening rates to the north might suggest the segment for the next rupture.

and c) we have projected the coseismic displacements and errors estimated by Anzidei et al. (2009), Table 1 to show the hangingwall subsidence and the footwall uplift. The maximum horizontal and vertical coseismic surface displacements detected at GPS stations were 10.4 ± 0.5 cm and -15.6 ± 1.6 cm, respectively.

Assuming an interseismic rate of 2.5 mm/y in the ductile unlocked part of the fault, as measured by GPS between L'Aquila

(AQUI) and Rome (INGR) stations (Fig. 5a); if we hypothesize a similar rate since the last earthquake that hit the area in 1703, about 75 cm of dilation between the locked and unlocked segments of the fault can be predicted. The L'Aquila April 6th 2009 earthquake generated a coseismic slip along the fault estimated in about 80 cm in the hypocentral plane (Chiarabba et al., 2009).

Low strain rate means that there is no stress accumulation at the surface, whereas a gradient of strain rate may indicate the activity of a structure at depth. Fig. 5a shows that at the surface, just east of AQUI, there was no interseismic motion, whereas a step of about 2.5 mm/y is present to the west of the site. This possibly indicates the activity of the prolongation below the BDT of the fault that caused the L'Aquila event, not associated with any significant strain rate gradient or jump at the surface (Fig. 4b and c). The transition to the higher strain rate (west of L'Aquila) means that the buried structure reaches the surface east of the faster interseismic movement (Fig. 5) due to the 45° westward dip of the fault. Therefore the stronger hazard is localized in an area where the strain rate was lower.

A numerical model was specifically built for the L'Aquila event. The model geometry, shown in Fig. 2b, is similar to that of the simplified conceptual model discussed above except for the blind geometry of the normal fault. If not otherwise specified, the tip of the fault is located at a depth of 2.5 km, consistently with seismic data. The model is conceptually similar to that described in Section 2 and the rheology is the same. However, in this case the displacement imposed during the interseismic stage is equal to 0.8 m. No further displacement is imposed during the coseismic stage (i.e., when the fault is unlocked). Fig. 6 shows the dilation and the principal stress axes during the interseismic and coseismic stages.

The distribution of foreshocks and aftershocks confirms the model (Fig. 7). In fact foreshocks are mostly concentrated along the area above the BDT, where a dilated band is inferred by the differential steady state motion in the lower ductile layer with respect to the locked upper part of the hangingwall. The aftershocks are, instead, well aligned along the activated upper segment of the normal fault (Fig. 7) and within the fallen hangingwall.

Fig. 8 shows the coseismic vertical displacement predicted by the numerical model at the surface (continuous lines in the figure), compared with the observed coseismic displacement measured by GPS at a magnified scale with respect to Fig. 5c. The agreement between predicted and measured vertical motions is reasonable, although the model predicts an area of subsidence slightly larger than that observed. The resulting deformation (Fig. 8) and the state of stress (compare Fig. 6e and f with Fig. 6c and d, respectively) is stable for Poisson's ratio in the range 0.27–0.33 or when the model is extended from the right instead than from the left. Variation of the depth of the fault tip point (in one case modelled as shallow as 1 km) does not cause dramatic changes in the model results. Fig. 6 shows results similar to those of Fig. 3, although the blind nature of the L'Aquila normal fault causes a shift of dilation from a depth of about 10 km to a depth of about 3 km from interseismic to coseismic stages.

4.2. Taiwan thrust belt

The island of Taiwan extends along the convergent boundary between Philippine Sea Plate and Eurasia. The subduction–collision process is the cause of repeated large earthquakes within the fold-and-thrust belt in Western Taiwan (Wu et al., 1997; Kaus et al., 2009). The large Chi-Chi earthquake (M_w 7.6, 20th September 1999, 8–10 km depth, Kao et al., 2000; Chang et al., 2000) resulted from the reactivation of the Chelungpu fault, a major N–S trending, westward verging thrust within the Taiwan accretionary prism (strike 5°, dip 34°, rake 65°, Chang et al., 2000). The fault kinematics displays a left-lateral transpressional component (Cattin et al., 2004).
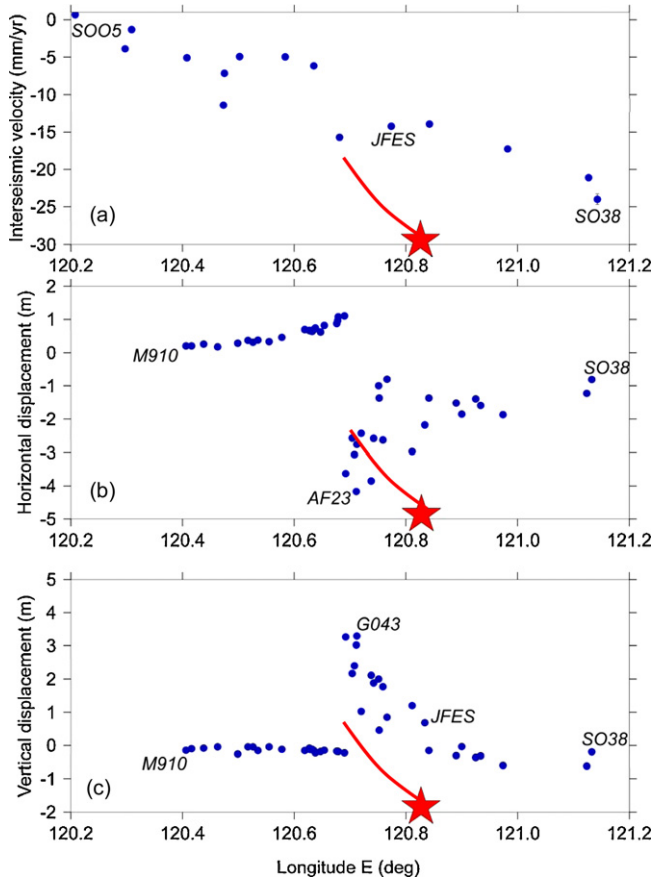
Fig. 10. Interseismic velocities (a), co-seismic horizontal (b) and vertical (c) displacements projected along the section shown in the previous figure perpendicular to the fault that generated the Chi-Chi earthquake. Error bars are smaller than dots. Star, location of the 20th September 1999 mainshock; the line represents a sketch of the fault section.

The interseismic rate across the thrust is inferred from the interseismic velocity field (Fig. 9a) reported in Table 4 of Yu et al. (2001) and the interseismic strain rate has been estimated in this paper with the method used for the L'Aquila case. Fig. 9b and c shows the maps of the principal axes of strain rate and of shortening rate, respectively. The epicentral area is characterized by an almost flat
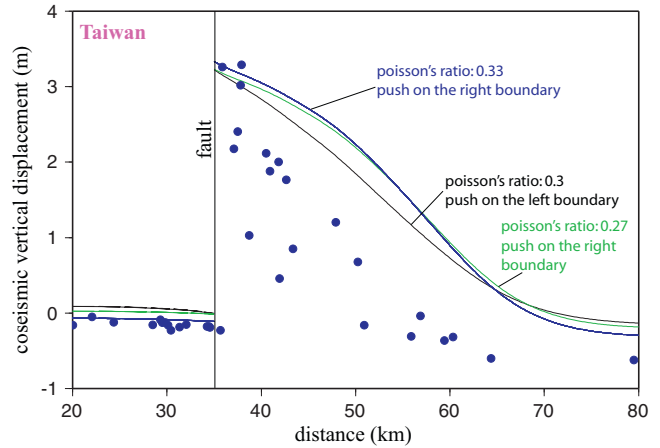

Fig. 12. Chi-Chi event: comparison between model and the observations. The continuous lines are the coseismic vertical motions predicted by the model (geometry shown in Fig. 2c). The blue dots are the coseismic displacements by GPS. Error bars are smaller than dots. (For interpretation of the references to colour in this figure legend, the reader is referred to the web version of the article.)

interseismic rate of 15 mm/y across the activated fault with an average shortening rate of $(250 \pm 10) \times 10^{-9}$ strain/y. The interseismic strain rate around the epicentral area is on average lower (Fig. 10a) than in neighbouring zones (Hsu et al., 2009). The rheology of central Taiwan is that of a typical continental crust (Zhou et al., 2003).

The earthquake broke the ground surface causing a 100-km-long rupture, mainly N–S trending. The coseismic GPS observations (Yu et al., 2001) show NW–NNW directed horizontal offsets of 1.1–9.1 m and vertical uplift of 1.2–4.4 m on the hanging wall. In contrast, much smaller SE–SEE directed horizontal movements of 0.1–1.5 m and slight subsidence of 0.02–0.26 m are found on the footwall. The projected displacements and errors are shown in Fig. 10b and c.

A numerical model was specifically built for the Chi-Chi event. The model is conceptually similar to that described in Section 2 and the rheology is the same. The geometry is shown in Fig. 2c. The interseismic displacement is equal to 6 m and it is imposed at the right boundary. No further displacement is imposed during the coseismic stage. Fig. 11 shows the dilation and the principal stress axes at interseismic stage and at the coseismic stage. Fig. 12 shows the coseismic vertical displacement predicted by the model at the

Taiwan
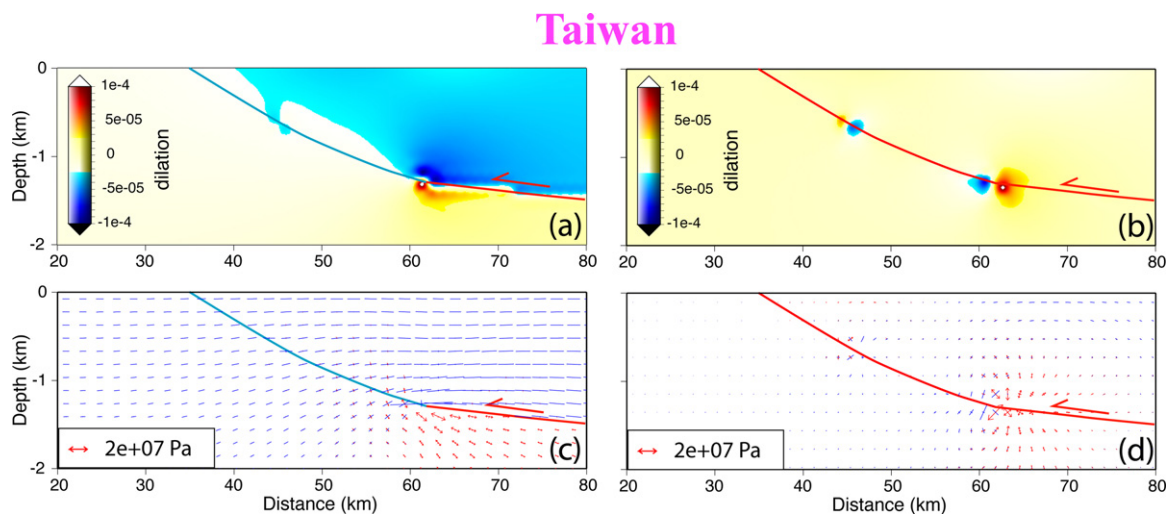
Fig. 11. Dilation (a,and b) and principal stress axes (c,and d) predicted at interseismic (a,and c) and coseismic (b,and d) stages by a model built to simulate the Chi-Chi event (geometry shown in Fig. 2c).

surface (continuous lines), compared with the observed coseismic displacement and errors measured by GPS. The agreement between predicted and measured vertical motions is reasonable, although, similar to the L'Aquila case, the model predicts an area of uplift slightly larger than that observed. As for the L'Aquila case, the displacement and stress predicted is rather stable also for rheological (change of the Poisson's ratio in the range 0.27–0.33, see Fig. 12) or geometric (shortening applied at the left boundary) variations. The dilation and state of stress predicted at interseismic and coseismic stages are consistent with those predicted by the conceptual model of Fig. 3, suggesting that our model is valid also for more complicated fault geometries.

4.3. Magnitude versus energy

On the basis of the previous analysis, we attempt here to investigate the relationship of the model in terms of energy radiation. As far as it concerns the L'Aquila example, assuming an average slip of $d = 0.75$ m, a fault width $W = 13$ km and fault length $L = 18$ km with a dip of $\theta = 43°$, we obtain a potential energy of $\Delta U = \rho g V d \sin \theta = \sim 2 \times 10^{13}$ J ($\rho = 2600$ kg/m³, $g = 9.8$ m/s², $V = LW^2 \sin \theta \cos \theta$), that has to be released into seismic radiation and other side effects. Assuming a radiation coefficient of $\alpha = 0.5$, the energy magnitude (Choy and Boatwright, 1995) is $M_e = 2/3 \log_{10}(\alpha \Delta U) = 5.75$ (for a radiation coefficient of 0.3 or 1, the energy magnitude is M_e 5.6 or M_e 5.95, respectively, comparable with the M_l 5.8). The same amount of potential energy corresponds to a seismic moment of 1.2×10^{18} N m, that is about half of the maximum geological moment. This suggests a weak behaviour of the fault, also indicated by the large difference between M_l and M_w. The potential energy released during the earthquake corresponds to the volume involved in the deformation (Fig. 6) above the BDT, neglecting the deformation occurring in the footwall. Computing the rise time and the particle velocity through simple mechanics we find $\sqrt{d/g} = 0.27$ s and $\sqrt{dg} = 2.6$ m/s, respectively, values that are in good agreement with the results of Cirella et al. (2009). In the hypothesis that gravity was the only force acting on the volume, the minimum shear stress required to keep the equilibrium would be $\sigma_s = \rho g V / 2WL = 83$ MPa, slightly less ($\sim$70%) than the maximum shear stress predicted by the rheological profile in the interseismic period. Thus the gravity force determining the instantaneous subsidence of the fault hangingwall possibly accounts for nearly all the total energy involved in the process whereas the internal strain in the brittle layer accounts for the remaining ($\sim$20%) energy. The long-lasting aftershocks in the area are interpreted as primarily related to the gradual settlement of the hangingwall to the new position, and distributed all over the volume within and above the previously dilated rocks (Fig. 3).

Considerations about the energy magnitude can be done also for the Chi-Chi thrust earthquake. Assuming an average slip of 6 m, a fault width $W = 35$ km, a fault length $L = 85$–105 km and a dip of 45° (Chen et al., 2003; Angelier et al., 2003), we obtain a potential energy of $\Delta U \sim 6.4 \times 10^{15}$ J. This value, for the compressional case, represents the increase in potential energy of the crustal volume affected by the coseismic deformation. In contrast to the energy budget in the tensional case, the potential energy represents the work done against gravity and it is additive to the seismic radiation, similarly to the terms related to the heating and to the permanent strain. In the specific case of Taiwan, the potential energy is approximately equal to the radiated energy (both approximately correspond to a magnitude of 7.6, using the Choy and Boatwright, 1995, formulation) and indicates a decrease in elastic strain energy (as in Savage and Walsh, 1978).

The usual assumption is that the energy during an earthquake is released by the failure of the fault plane. In the L'Aquila example,
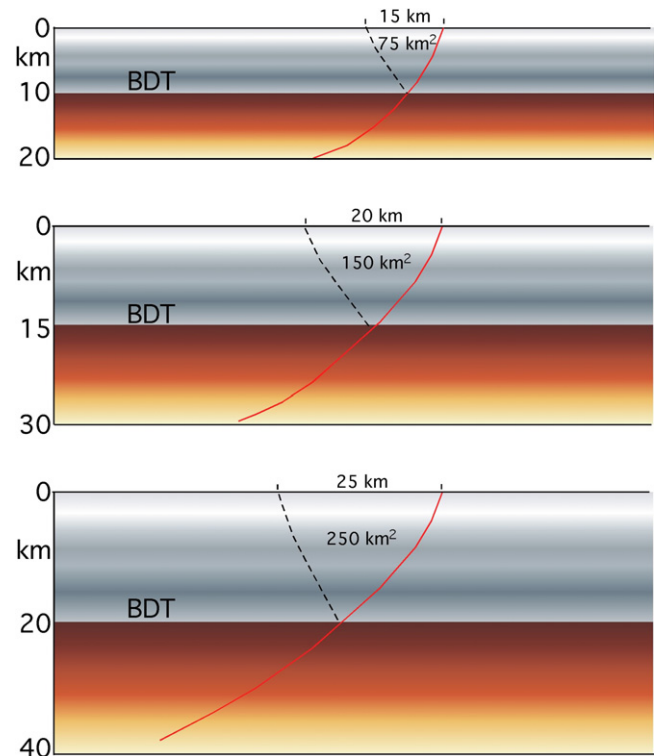

Fig. 13. Assuming similar fault length and accumulated slip, the deepening of the brittle–ductile transition depth determines an increase of the volume involved during the earthquake, and hence of its magnitude. High geothermal flux generates a shallow BDT, i.e., smaller volume above BTD and lower seismic energy release.

the magnitude ($M_l = 5.8$) appears as the energy dissipated by the fall of the entire volume crashing onto the dilated band ($M_e = 5.75$), rather than the failure of the fault plane ($M_w = 6.3$–6.4). For the Chi-Chi event, the energy radiated ($M_w = 7.6$) is similar to the one that can be computed with the expulsion of the hangingwall above the BDT ($M_e = 7.6$), and smaller than what predicted by the fault plane dimension (M 7.8). Usually, the seismic moment and the moment magnitude are computed on the basis of the area of the activated fault plane. We wonder whether it could be more realistic (and helpful) to compute the seismic moment and magnitude on the basis of the involved volume rather than on the fault area. The volume would be the one confined by the activated fault plane, the BDT at depth, and the conjugate band above it in the hangingwall. This would be a quite different perspective on the origin and energy radiation of the seismic waves.

5. Conclusions

We have shown that the BDT can play a relevant role in controlling the activation of a fault and possibly in determining the seismic cycle. The interseismic stage is characterized by steady-state shear in the ductile part of the fault (shear zone at depth), while the upper brittle segment is locked. The coseismic stage allows the brittle part to move; in this layer the deformation gradually decreases during the postseismic or afterslip stage, which may last several years (Marone et al., 1991). In this model the contrasting deformation style across the BDT acts as a switch, turning on and off the seismogenic segment of the fault. This contrasting behaviour should generate a sort of spring-like evolution at the transition between the two domains. The conflicting behaviour of the brittle and ductile layers crossed by a seismogenic fault predicts a strain partitioning at the BDT, which is different in the tensional or compressional settings.

In crustal environments, at the BDT, a dilated volume forms at the base of a locked normal fault during the interseismic period. Once the shear stress becomes larger than the fault strength, besides the newly created "empty" weak space at the lower tip of the fault, the hangingwall suddenly subsides to rejoin the displaced segment, generating the mainshock (Fig. 1).

An opposite behaviour is predicted for thrust faults that, during the interseismic period, should be characterized by focussed compression at the transition between the ductile and brittle layers (Fig. 1). When the accumulated energy provides a maximum horizontal stress sufficient to exceed the friction on the locked brittle part of the thrust, the hangingwall is expelled forward and upward.

The motion of an active fault at the BDT can be compared to a spring anchored to the ductile and brittle parts of the hangingwall. During the interseismic period, along a normal fault the spring is elongated, whereas it is compressed in the convergent setting. During the coseismic stage, the two systems reverse, i.e., the spring is compressed along a normal fault, while it is elongated along a thrust (Fig. 1).

Once the hangingwall settles, a new cycle of interseismic loading can start again. The rupture of rocks in general requires more energy under compression with respect to tension. Moreover, more energy is required to uplift the hangingwall of a thrust with respect to the passive subsidence of the hangingwall of a normal fault. This may also explain the larger energy radiation in compressive environments. The computation made for the normal faulting and thrust examples shows that the energy released by the instantaneous subsidence or uplift of the fault hangingwall matches quite well the observed magnitude, and it is larger when the deformation goes against gravity.

The volume deformed during the coseismic stage appears as a fundamental value in controlling the energy released during an earthquake, and the volume increases as the BDT deepens (Fig. 13). Therefore, at a given fault length and slip rate, bigger earthquakes are expected to be associated with a deeper level of the BDT. Moreover, multiple BDT transitions may occur within a crustal or lithospheric thickness as a function of the involved lithologies.

Finally, the model indicates that moving along strike of a seismogenic fault, the interseismic period is characterized by slow or no motion along those segments which are locked in the brittle crust and are tectonically loading (e.g., Fig. 4). The area close to the L'Aquila epicenter was characterized by interseismic rates close to zero (Fig. 4b). Therefore, along an active fault, the strain rate computed by GPS should be lower than average in areas more prone to an earthquake. Using the L'Aquila earthquake as an example, we show that, knowing the kinematic and mechanical crustal parameters of an active area, we might arrive to predict the specific region where a fault is stressed by active slip at ductile layers.

Acknowledgments

References

Amato, et al., 1998. The 1997 Umbria-Marche, Italy, earthquake sequence: a first look at the main shocks and aftershocks. Geophys. Res. Lett. 25 (15), 2861–2864.

Angelier, J., Lee, J.C., Chu, H.T., Hu, J.C., 2003. Reconstruction of fault slip of the September 21st, 1999, Taiwan earthquake in the asphalted surface of a car park, and coseismic partitioning. J. Struct. Geol. 35, 345–350.

Anzidei, M., Boschi, E., Cannelli, V., Devoti, R., Esposito, A., Galvani, A., Melini, D., Pietrantonio, G., Riguzzi, F., Sepe, V., Serpelloni, E., 2009. Coseismic deformation of the destructive April 6, 2009 L'Aquila earthquake (central Italy) from GPS data. Geophys. Res. Lett. 36, L17307, doi:10.1029/2009GL039145.

Axen, G.J., 1999. Low-angle normal fault earthquakes and triggering. Geophys. Res. Lett. 26, 3693–3696, doi:10.1029/1999GL005405.

Barba, S., Carafa, M.C., Mariucci, M.T., Montone, P., Pierdominici, S., 2010. Present-day stress-field modelling of southern Italy constrained by stress and GPS data. Tectonophysics 482 (1–4), 293–304, doi:10.1016/j.tecto.2009.10.017.

Barba, S., Carafa, M.C., Boschi, E., 2008. Experimental evidence for mantle drag in the Mediterranean. Geophys. Res. Lett. 35, L06302, doi:10.1029/2008GL033281.

Bird, P., 1978. Finite element modeling of lithosphere deformation: the Zagros collision orogeny. Tectonophysics 50, 307–336.

Burrato, F., Ciucci, F., Valensise, G., 2003. An inventory of river anomalies in the Po Plain, Northern Italy: evidence for active blind thrust faulting. Ann. Geophys. 46 (5), 865–882.

Carminati, E., Doglioni, C., Barba, S., 2004. Reverse migration of seismicity on thrusts and normal faults. Earth Sci. Rev. 65, 195–222.

Cattin, R., Avouac, J.P., 2000. Modeling mountain building and the seismic cycle in the Himalaya of Nepal. J. Geophys. Res. 105 (B6), 13389–13407.

Cattin, R., Loevenbruck, A., Le Pichon, X., 2004. Why does the co-seismic slip of the 1999 Chi-Chi (Taiwan) earthquake increase progressively northwestward on the plane of rupture? Tectonophysics 386, 67–80, doi:10.1016/j.tecto.2004.05.002.

Chang, C.H., Wu, Y.M., Shin, T.C., Wang, C.Y., 2000. Relocation of the 1999 Chi-Chi earthquake in Taiwan. TAO 11 (3), 581–590.

Chen, W.-S., Chen, Y.-G., Shih, L., Hang, L., Sung, L., 2003. Thrust-related river terrace development in relation to the 1999 Chi-Chi earthquake rupture, Western foothills, central Taiwan. J. Asian Earth Sci. 21, 473–480.

Chiarabba, et al., 2009. The 2009 L'Aquila (central Italy) MW6.3 earthquake: main shock and aftershocks. Geophys. Res. Lett. 36, L18308, doi:10.1029/2009GL039627.

Chiarabba, C., Jovane, L., Di Stefano, R., 2005. A new view of Italian seismicity using 20 years of instrumental recordings. Tectonophysics 395, 251–268.

Choy, G.L., Boatwright, J.L., 1995. Global patterns of radiated seismic energy and apparent stress. J. Geophys. Res. 100 (B9), 18205–18228, doi:10.1029/95JB01969.

Cirella, A., Piatanesi, A., Cocco, M., Tinti, E., Scognamiglio, L., Michelini, A., Lomax, A., Boschi, E., 2009. Rupture history of the 2009 L'Aquila (Italy) earthquake from non-linear joint inversion of strong motion and GPS data. Geophys. Res. Lett. 36, L19304, doi:10.1029/2009GL039795.

Collettini, C., Niemeijer, A., Viti, C., Marone, C., 2009. Fault zone fabric and fault weakness. Nature 462 (7275), 907–910, doi:10.1038/nature08585.

Collettini, C., Sibson, R.H., 2001. Normal faults, normal friction? Geology 29 (10), 927–930.

Devoti, R., Riguzzi, F., Cuffaro, M., Doglioni, C., 2008. New GPS constraints on the kinematics of the Apennine subduction. Earth Planet Sci. Lett. 273 (1–2), 163–174.

Di Luccio, F., Ventura, G., Di Giovambattista, R., Piscini, A., Cinti, F.R., 2010. Normal faults and thrusts re-activated by deep fluids: the 6 April 2009 M_w 6.3 L'Aquila earthquake, central Italy. J. Geophys. Res. 115 (B06315), 15, doi:10.1029/2009JB007190.

Fialko, Y., 2004. Evidence of fluid-filled upper crust from observations of postseismic deformation due to the 1992 M_w 7.3 Landers earthquake. J. Geophys. Res. 109, B08401, doi:10.1029/2004JB002985.

Frank, F.C., 1965. On dilatancy in relation to seismic sources. Rev. Geophys. 3, 485–503.

Hsu, Y.-J., Yu, S.-B., Simons, M., Kuo, L.-C., Chen, H.-Y., 2009. Interseismic crustal deformation in the Taiwan plate boundary zone revealed by GPS observations, seismicity, and earthquake focal mechanisms. Tectonophysics 479 (1–2), 4–18.

Jonsson, S., Segall, P., Pedersen, R., Bjornsson, G., 2003. Post-earthquake ground movements correlated to pore-pressure transients. Nature 424, 179–183, doi:10.1038/nature01776.

Kao, H., Chen, R.Y., Chang, C.H., 2000. Exactly where does the 1999 Chi-Chi earthquake in Taiwan nucleate? Hypocenter relocation using the Master Station Method. TAO 11 (3), 567–580.

Kaus, Boris, J.P., Liu, Y., Becker, T.W., Yuen, D.A., Shi, Y., 2009. Lithospheric stress-states predicted from long-term tectonic models: influence of rheology and possible application to Taiwan. J. Asian Earth Sci. 36, 119–134, doi:10.1016/j.jseaes.2009.04.004.

Kreemer, C., Holt, W.E., Haines, A.J., 2002. The global moment rate distribution within plate boundary zones. Geodyn. Ser. 30, 173–189.

Marone, C.J., Scholtz, C.H., Bilham, R., 1991. On the mechanics of earthquake afterslip. J. Geophys. Res. 96 (B5), 8441–8452.

Masterlak, T., Wang, H.F., 2002. Transient stress-coupling between the 1992 Landers and 1999 hector mine, California. Earthquakes Bull. Seism. Soc. Am. 92 (4), 1470–1486.

Melosh, H.J., Williams, C.A., 1989. Mechanics of graben formation in crustal rocks—a finite-element analysis. J. Geophys. Res. 94, 13961–13973.

Meltzner, A.J., Sieh, K., Abrams, M., Agnew, D.C., Hudnut, K.W., Avouac, J.P., Natawidjaja, D., 2006. Uplift and subsidence associated with the great Aceh–Andaman earthquake of 2004. J. Geophys. Res. 111 (B02407), doi:10.1029/2005JB003891.

Nuchter, J.A., Stockhert, B., 2008. Coupled stress and pore fluid pressure changes in the middle crust: vein record of coseismic loading and postseismic stress relaxation. Tectonics 27 (TC1007), doi:10.1029/2007TC002180.

Peresan, A., Kossobokov, V., Romashkova, L., Panza, G.F., 2005. Intermediate-term middle-range earthquake predictions in Italy: a review. Earth Sci. Rev. 69, 97–132.

Peltzer, G., Rosen, P., Rogez, F., Hudnut, K., 1998. Poroelastic rebound along the Landers 1992 earthquake surface rupture. J. Geophys. Res. 103 (B12), 30131–30145.

Pingue, F., De Natale, G., 1993. Fault mechanism of the 40 seconds subevent of the 1980 Irpinia (Soutehrn Italy) earthquake from levelling data. Geophys. Res. Lett. 20 (10), 911–914.

Riguzzi, F., Pietrantonio, G., Devoti, R., Atzori, S., Anzidei, M., 2009. Volcanic unrest of the Colli Albani (central Italy) detected by GPS monitoring test. Phys. Earth Planet Int., doi:10.1016/j.pepi.2009.07.012.

Rutter, E.H., 1986. On the nomenclature of mode of failure transitions in rocks. Tectonophysics 122, 381–387.

Savage, J.C., 1983. A dislocation model of strain accumulation and release at a subduction zone. J. Geophys. Res. 88, 4984–4996.

Savage, J.C., Walsh, J.B., 1978. Gravitational energy and faulting. Bull. Seism. Soc. Am. 68 (6), 1613–1622.

Scholtz, C.H., 1990. The Mechanics of Earthquakes and Faulting. Cambridge University Press, Cambridge/New York (Ref. QE534.2.S37).

Shen, Z.K., Jackson, D.D., Ge, B.X., 1996. Crustal deformation across and beyond the Los Angeles basic from geodetic measurements. J. Geophys. Res. 101, 27957–27980.

Sieh, K., Natawidjaja, D.H., Meltzner, A.J., Shen, C.-C., Cheng, H., Li, K.-S., Suwargadi, B.W., Galetzka, J., Philibosian, B., Edwards, R.L., 2008. Earthquake supercycles inferred from sea-level changes recorded in the corals of west Sumatra. Science 322 (5908), 1674–1678, doi:10.1126/science.1163589.

Stein, S., Wysession, M., 2003. Introduction to Seismology, Earthquakes, and Earth Structure. Blackwell Publishing.

Thatcher, W., Rundle, J.B., 1979. A model for the earthquake cycle in underthrust zones. J. Geophys. Res. 84, 5540–5556.

Tullis, J.A., 1979. High-temperature deformation of rocks and minerals. Rev. Geophys. 17 (6), 1137–1154.

Vezzani, L., Ghisetti, F., 1998 Carta Geologica dell'Abruzzo, scala 1/100.000, Regione Abruzzo, Selca.

Wu, F.T., Rau, R.J., Salzberg, D., 1997. Taiwan orogeny: thin-skinned or lithospheric collision? Tectonophysics 274, 191–220.

Yu, S.B., Kuo, L.C., Hsu, Y.J., Su, H.H., Liu, C.C., Hou, C.S., Lee, J.F., Lai, T.C., Liu, C.C., Liu, C.L., Tseng, T.F., Tsai, C.S., Shin, T.C., 2001. Preseismic deformation and coseismic displacements associated with the 1999 Chi-Chi, Taiwan earthquake. Bull. Seismol. Soc. Am. 91, 995–1012.

Zhou, D., Yub, H.-S., Xua, H.H., Shia, X.B., Chou, Y.W., 2003. Modeling of thermorheological structure of lithosphere under the foreland basin and mountain belt of Taiwan. Tectonophysics 374, 115–134.